Adaptive High-Dynamic Range Three-Dimensional Shape Measurement Using DMD Camera

SHOU-BO ZHAO[ID], LI-YUAN LIU, AND MING-YANG MA

The Higher Educational Key Laboratory for Measuring and Control Technology and Instrumentations of Heilongjiang Province, Harbin University of Science and Technology, Harbin 150080, China

Corresponding author: Shou-Bo Zhao (shoubozh@126.com)

ABSTRACT The phase shifting profilometry for the object with high reflectivity variation is an important issue in equipment manufacturing, medical sciences, and entertainment industry. To address the problem, in this paper, an adaptive high dynamic range three-dimensional shape measurement using DMD camera is proposed. By analyzing the imaging characteristics affected by bidirectional reflectance distribution function and the crosstalk on CCD chip, the strategy that DMD modulation function is determined to avoid saturation prior to the acquisition of phase shifting images is applied. To verify the performance of the proposed method, the B/W flat checkerboard, the plastic button, and the metal slice with high-reflectivity variation are measured to reconstruct the 3D model. The experimental results show that our proposed method can correct the deformed phase which is caused by the image saturation. Finally, the measuring accuracy of the proposed method is given. Compared with two common high-dynamic range measurement methods, our proposed method has the advantages in the accuracy and the efficiency.

INDEX TERMS Shape measurement, dynamic range, optical saturation, micromirrors.

I. INTRODUCTION

3D measurement technology plays an important role in equipment manufacturing, medical sciences and entertainment industry [1]–[3]. Phase shifting profilometry which can acquire more point cloud data has significant advantage in the efficiency and effectiveness of the measurement, compared with other 3D measurement technologies such as coordinate measuring machine, laser distance measuring, speckle interference and stereo vision [4], [5]. However, the phase shifting profilometry is confronted with the challenge of measuring the object with high reflectivity variation [6]–[8]. Once strong light from high reflective surface generates saturation region in image sensor, fringe images are unable to record the true intensity variation of the structured light deformed by the object surface [9]. Thereby, the depth information is not accurately determined from the phase map. The type of form errors results in the surface deformation or holes in the 3D

reconstructed shape. Whereas weak light from low reflective surface generates dark region in image sensor, same result happens here. Since the visibility of low reflective surface is ensured first, major challenge focuses on the saturation avoidance [10].

To meet this challenge, many methods were proposed in resent years. One type of methods is dual-camera structured light which avoids saturation by compositing images from different viewing angles [11]–[13]. However, the position error caused by image registration in dual-camera structured light measurement is inevitable. Because dual-camera-projector can be regarded as two single-camera-projector structures, a method which can employ single-camera-projector structure to avoid image saturation from high reflective surface is more valuable. Another type of methods calculates phase of saturated points with corresponding unsaturated value in other phase shifting images to avoid saturation [14]–[16]. However, the saturation region which can be calculated is limited by the spatial period of phase shifting fringe and the reflectivity of corresponding surface.

The associate editor coordinating the review of this manuscript and approving it for publication was Alba Amato.

Besides above methods, high dynamic range (HDR) imaging methods are widely used to avoid saturation in 3D shape measurement due to the advantages in the adaptability of reflected luminance and the flexibility of dynamic range [17], [18]. In most of high dynamic range imaging methods, multiple sets of phase shifting images need to be captured at different exposures. Exposure variation means including the adjustment of aperture, the control of CCD exposure time and the intensity modulation of fringe projection are employed in [19]–[21]. However, the adjustment of aperture cannot quantitatively vary the exposure. The control of CCD exposure time requires extensive efforts on gamma correction. The same as the adjustment of aperture and the control of CCD exposure time, the intensity modulation of fringe projection consumes great time at the acquisition of the phase shifting images and the generation of composite images [22]–[24].

Since digital micromirror device (DMD) camera as high dynamic range imaging system can quantitatively attenuate the intensity from reflective surface by controlling individual DMD pixel on corresponding image position, we employ DMD camera to implement 3D shape measurement for the object with high reflectivity variation in this paper [25], [26]. This paper is organized as follow: Imaging characteristics of the surface with high reflectivity variation is studied by analyzing the bidirectional reflectance distribution function and the crosstalk on CCD chip. Whereafter, we propose an adaptive high dynamic range 3D measurement method that DMD is modulated to avoid saturation prior to the acquisition of phase shifting images. Finally, the experimental procedures and results are given to verify the performance of proposed method.

II. METHOD

A. IMAGING CHARACTERISTICS OF THE OBJECT WITH HIGH REFLECTIVITY VARIATION

The high-reflectivity-variation object exists extensively in 3D shape measurement application. Simple object, such as black and white flat checkerboard, consists of high reflective surface and low reflective surface [10], [17]. High reflective surface generates strong light to form the bright region in the image. On the contrary, low reflective surface generates weak light to form the dark region in the image. Complex objects such as plastic button and metal slice, are affected by the incident angle of light source, the curvature and roughness of reflective surface. Their reflectivity variation is commonly determined by bidirectional reflectance distribution function (BRDF) [11], [12]. Fig.1 shows BRDF model and imaging mechanism on pixel array. It is well known that the specular lobe and the specular spike in BRDF are the major factors causing the image saturation. However, crosstalk glare as a third factor is seldom mentioned. It is generated by the optical and electrical crosstalk which is defined as the unwanted output signal of the diffused photocarriers from neighboring pixels. The crosstalk theory has been widely recognized in the photoelectron imaging field [27], [28]. Our group also found the phenomenon that the light intensity of
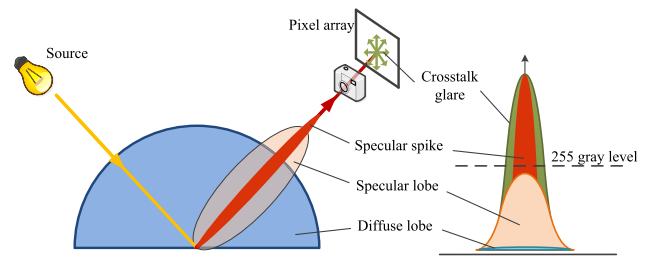

FIGURE 1. BRDF model and imaging mechanism on pixel array.
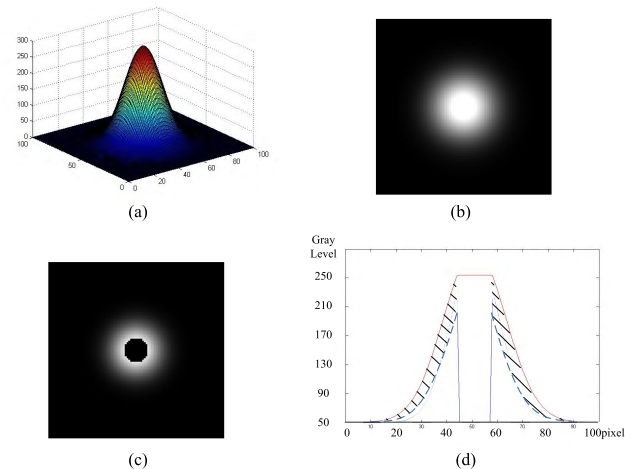

FIGURE 2. The experimental phenomenon about crosstalk glare. (a) Light intensity distribution at the reflected specular-spike direction. (b) The saturation image captured by CCD. (c) The captured image after the removal of central intensity. (d) The cross-sections of (b) and (c).

surrounding pixels is decreasing with the specular spike on the central pixels being removed by spatial light modulator (SLM), as shown in Fig.2 [29]. Fig.2(a) is predetermined light intensity at the reflected specular-spike direction from BRDF surface. Fig.2(b) is the corresponding saturation image captured by CCD directly. Fig.2(c) is the captured image after the removal of central intensity. The SLM as an array switch is mounted on front of image sensor. By closing the switches before central pixels, the light intensity of surrounding pixels is removed. The cross-sections of Fig.2(b) and Fig.2(c) are represented by red solid line and blue dash line, as shown in Fig.2(d). The shadow area is regarded as the crosstalk glare intensity which has been eliminated after the removal of central intensity. The rest of light intensity (blue line) contains the diffuse lobe portion and specular lobe portion. In other words, the crosstalk glare depends on the light intensity of the central pixel. However, the diffuse lobe, the specular lobe and the specular spike from the reflective surface don't have the characteristic. In addition, the intensity of the crosstalk glare is decreasing with the distance from the central pixel. The bigger the light intensity of the central pixel is, the wider the diameter of the crosstalk glare is.

In a word, for the most of metal parts and plastic products in manufacturing industry, above-mentioned factors will greatly
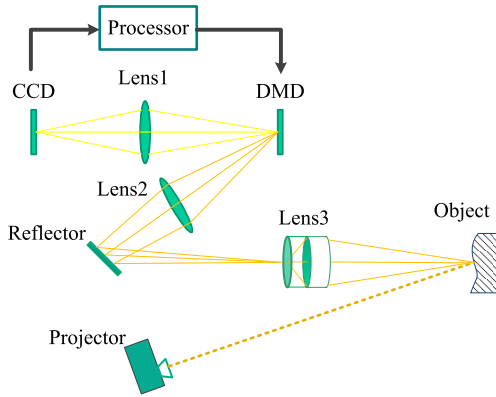
FIGURE 3. The schematic of proposed 3D measurement system.

FIGURE 4. 5-grating pattern which is composed of square-ring grating, top grating, bottom grating, left grating and right grating.

FIGURE 5. The changes of various moiré images on the procedure of the pixel-to-pixel correspondence alignment.

widen the broad range of luminance on the surface. Once the broad range of luminance on the surface exceeds the dynamic range of image sensor in phase shifting profilometry, the contradiction between the saturation avoidance in bright regions and the fringe visibility in dark regions emerges. To resolve the contradiction, adaptive high dynamic range techniques using DMD camera is presented in this paper. Furthermore, assuming that the crosstalk glare is small enough to be ignored when the qualified off-the-shelf CCD works in the unsaturated state, the phase-shifting image acquisition should be carried out after the saturation is avoided completely.

B. MAPPING BETWEEN DMD AND CCD

Fig.3 is the schematic of adaptive high dynamic range 3D measurement system. The system is composed of fringe projector, CCD, DMD, image processor and three imaging lenses (Lens1, Lens2 and Lens3). Fringe projector is employed to project the phase shifting patterns on the object surface. DMD is a 2D array optoelectronic modulator in which every pixel has two stable mirror states (+12° tilt and −12° tilt) to control the direction of scene ray with high precision over space and time. PC as imaging processor handles the camera image and controls the DMD pattern. Lens3 as an objective lens determines the measured object size. Lens2 as the relay lens images the focal plane of Lens3 to the DMD plane. Lens1 as the relay lens focuses reflected ray from DMD to CCD plane. DMD mounted on intersection of two optical axis can quantitatively reduces incident intensity from object and reflects the processed ray to CCD by 24°. By the light modulation of the DMD, adaptive high dynamic range 3D measurement will be performed.

Before adaptive high dynamic range 3D measurement, the first thing is to achieve accurate pixel-to-pixel alignment between DMD and CCD. The pixel-to-pixel alignment between DMD and CCD involves six degree of freedom (DoF) adjustments including three linear displacements on the horizontal axis x, the vertical axis y, the optical axis z and three angular displacements on pitch angle, yaw angle, roll angle. Lens1 images the DMD plane to

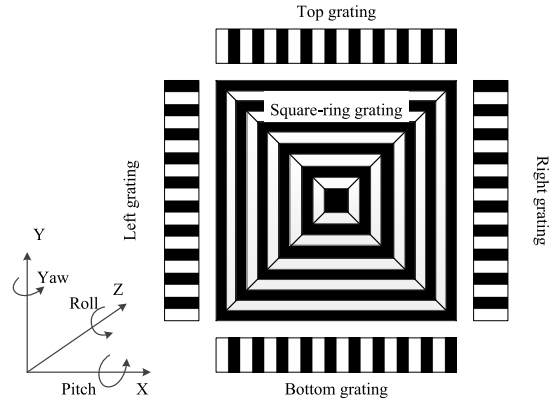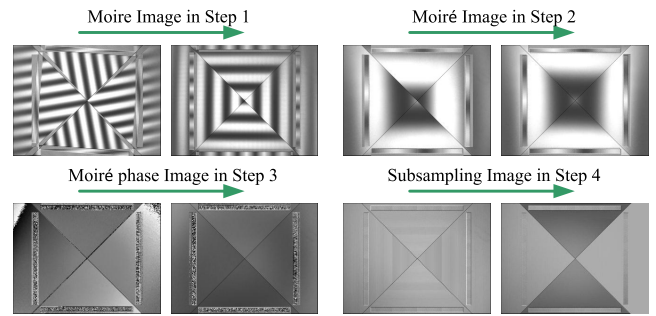CCD plane. In the object-image conjugate architecture, the six DoF adjustments can be achieved by using the moiré fringe method. Here, the DMD can be regarded as one grating by controlling the micro mirror array to form black and white line patterns, and the CCD can be regarded as another grating by using the subsampling technique. When the image of DMD pattern is superposed on the CCD pattern, the produced moiré fringe will appear in the computer screen. A special pattern called 5-grating pattern is synchronously displayed on the DMD and CCD for monitoring and adjusting the six DoF displacements, as is shown in Fig.4. Two gratings with the same frequency in x-axis direction are respectively placed in the top and bottom of the pattern. Two gratings with the same frequency in y-axis direction are respectively placed in the left and right of the pattern. And a square-ring grating is placed in the center of the pattern.

Figure 5 is the changes of various observed images on the procedure of the pixel-to-pixel correspondence alignment. In the computer screen, three observed images called moiré image, moiré phase image and subsampling image are used to monitor six-axis adjustment. Moiré image $I_m(x, y)$ is obtained by

$$I_m^i(x, y) = I\left(\frac{fL}{N} \cdot Floor(\frac{Nx}{fL}) + \frac{iL}{N}, \frac{fL}{N} \cdot Floor(\frac{Ny}{fL}) + \frac{iL}{N}\right)$$

$$(1)$$

where function *Floor*[●] is to get the integer towards minus infinity. (x, y) is the CCD pixel coordinate. $I(x, y)$ is the original moiré image captured by CCD. The symbol L and N are the numbers of the CCD pixel and DMD pixel in the mapping. The symbol f denotes the period of original grating fringe. Shifting phase in i th moiré image is $2i\pi/f$, $i = 1, 2, \ldots, f$.

Moiré phase image $\varphi(x, y)$ can be obtained by

$$\varphi(x, y) = \arctan\left(\frac{\sum_{i=1}^{f} I_m^i \cdot \sin(2i\pi/f)}{\sum_{i=1}^{f} I_m^i \cdot \cos(2i\pi/f)}\right) \quad (2)$$

Subsampling image $I_S(x, y)$ can be obtained by

$$I_s(x, y) = I\left(\frac{fL}{2N} \cdot Floor(\frac{2Nx}{fL}) + Mod(2Nx, fL),\right.$$
$$\left.\frac{fL}{2N} \cdot Floor(\frac{2Ny}{fL}) + Mod(2Ny, fL)\right) \quad (3)$$

where function *Mod*[*dividend*, *divisor*] is to get the remainder.

The pixel-to-pixel correspondence alignment has four steps as follows. In the first step, by observing the moiré image, the roll angle is adjusted to obtain the intermediate result that the moiré fringe parallels the original grating fringe. In step2, the pitch angle is adjusted to make the moiré phases of the top grating and the bottom grating identical, and yaw angle is adjusted to make the moiré phases of the left grating and the right grating identical in the moiré image. Two phase differences are displayed in real time. In step3, by observing the moiré phase image, the paraxial magnification and z displacement along the optical axis are adjusted to make moiré phase distribution uniform. At this moment, the frequency difference between the CCD and DMD equals to zero. In step4, by observing the subsampling image, x-axis and y-axis displacements are adjusted to eliminate the initial phases of moiré fringe. The pixel-to-pixel correspondence alignment is completed by the four-step adjustment, which is discussed in detail in [30].

C. ADAPTIVE HIGH DYNAMIC RANGE 3D MEASUREMENT TECHNIQUE

There are two types of mappings from DMD to CCD: one DMD pixel being assigned to one CCD pixel, and multiple DMD pixels being assigned to one CCD pixel. In case that one DMD pixel is assigned to one CCD pixel, the enhancement of dynamic range can be achieved by modulating the DMD bit level. When DMD pixel value $DMD(x, y)$ ranges from 0 to 255 in 8 bit levels, the modulation function is expressed as:

$$M(x, y) = DMD(x, y)/255 \quad (4)$$

In this case, the dynamic range of proposed DMD camera system DR_{system} will be enhanced to:

$$DR_{system} = 255 \cdot DR_{CCD} \quad (5)$$
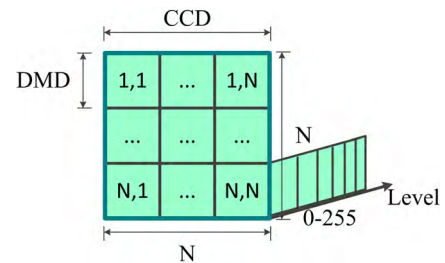
where DR_{CCD} denotes the dynamic range of CCD.

FIGURE 6. N∗N DMD pixels being assigned to one CCD pixel.

In another case that multiple DMD pixels are assigned to one CCD pixel, the dynamic range is affected by DMD pixel value and the number of corresponding DMD pixels. Fig.6 shows the diagram of $N \times N$ DMD pixels being assigned to one CCD pixel. The modulation function is expressed as

$$M(x, y) = \frac{1}{255^{N \times N}} \sum_{i=1}^{N} \sum_{j=1}^{N}$$
$$\times DMD(N \times x + i - N, N \times y + j - N) \quad (6)$$

In this case, the dynamic range of proposed DMD camera system DR_{system} will be further enhanced to:

$$DR_{system} = 255 \cdot N^2 \cdot DR_{CCD} \quad (7)$$

One DMD pixel being assigned to one CCD pixel can be regarded as the second case that N is equal to one. Due to the limitation of DMD pixel number, N need to be selected based on a tradeoff between the dynamic range and the image resolution of DMD camera system.

The determination of the modulation function is crucial to achieve high dynamic range 3D measurement. At the beginning, the modulation function $M^0(x, y)$ is set to one, and the light with lowest uniform brightness is projected onto the object surface. The aperture and exposure time are adjusted to ensure the dark surface clear. Then the light with the highest uniform brightness is projected onto the object surface. Look for the saturation points throughout the captured image. The corresponding value in the modulation function is multiplied by a scale factor $p < 1$. Repeat to look for saturation points throughout the new image and set modulation function until the there is no saturation in the image.

The modulation function $M^k(x, y)$ in k th time can be given by

$$M^k(x, y) = \begin{cases} M^{k-1}(x, y) & I^k(x, y) < 255 \\ M^{k-1}(x, y) \cdot p & I^k(x, y) = 255 \end{cases} \quad (8)$$

where $M^{k-1}(x, y)$ is the modulation function last time, and $I^k(x, y)$ is the captured image in k th time. If the saturation points still remain in the image when the element in the modulation function is reduced to the minimum $1/(255 \cdot N^2)$, it is necessary to increase N value in the pixel-to-pixel alignment.

In this research, we employ four-step phase shifting algorithm to calculate the wrapped phase. The fringe pattern

images with a phase shift $\pi/2$ is expressed as

$$I_1 = a(x, y) + b(x, y) \cos[\phi(x, y)] \tag{9}$$

$$I_2 = a(x, y) + b(x, y) \cos[\phi(x, y) + \pi/2] \tag{10}$$

$$I_3 = a(x, y) + b(x, y) \cos[\phi(x, y) + \pi] \tag{11}$$

$$I_4 = a(x, y) + b(x, y) \cos[\phi(x, y) + 3\pi/2] \tag{12}$$

where (x, y) is the CCD pixel coordinate, $a(x, y)$ is the background intensity, and $b(x, y)$ is the intensity amplitude. Regardless of the saturation of image sensor, the desired phase $\phi(x, y)$ is calculated by

$$\phi(x, y) = \arctan[(I_2 - I_4)/(I_1 - I_3)] \tag{13}$$

The wrapped phase $\phi(x, y)$ is not affected by the variation of $a(x, y)$ and $b(x, y)$ in the absence of image saturation. $b(x, y)$ can represent the intensity amplitude of pixels which are independent of one another, i.e., $b(x, y)$ can include the diffuse lobe, the specular lobe and the specular spike except the crosstalk glare. Therefore, the crosstalk glare should be removed to achieve accurate 3D measurement.

Assuming that the saturation in the image is eliminated in the K th time, the phase shifting fringe patterns are projected onto the object surface. Four fringe images after the DMD modulation can be rewritten as:

$$I_1^K = M^K(x, y)\{a(x, y) + b(x, y) \cos[\phi(x, y)]\} \tag{14}$$

$$I_2^K = M^K(x, y)\{a(x, y) + b(x, y) \cos[\phi(x, y) + \pi/2]\} \tag{15}$$

$$I_3^K = M^K(x, y)\{a(x, y) + b(x, y) \cos[\phi(x, y) + \pi]\} \tag{16}$$

$$I_4^K = M^K(x, y)\{a(x, y) + b(x, y) \cos[\phi(x, y) + 3\pi/2]\} \tag{17}$$

As (14-17) indicate, we can obtain the following: All pixels in image coordinate have respective modulation coefficient to avoid the saturation. The modulation coefficients of four fringe images are identical on arbitrary pixel to ensure the calculation of wrapped phase $\phi(x, y)$. We assume that the crosstalk in 255 gray level is small enough to be ignored, i.e., 255 gray level is the perfect state off-the-shelf CCD work in. Thus the crosstalk glare is removed from four fringe images by avoiding the image saturation. By two-frequency phase unwrapping algorithm, adaptive high dynamic range 3D measurement can be implemented.

III. EXPERIMENT
A. EXPERIMENTAL SETUP AND SYSTEM CALIBRATION
For verifying our proposed method, we construct the experimental setup, as shown in Fig.7. Here a digital light processing projector (TI-LightCrafter) with a resolution of 608×640. CCD (Teli-BU30) allows for 8 bits per pixel (bpp) of precision in RAW mode and a resolution of 768×576; each CCD is 7.4×7.4 microns in size. DMD (TI-WXGA0.45) provides 8bpp and a resolution of 1140×912; each mirror element is 7.6×7.6 microns. The vertical magnification of lens1 is adjustable in the range from 0.3 to 3.5; the focal length in the image space is approximately 100mm. Lens3 (Schneider Kreuznach Xenon 0.95/17) can be selected according to the measured object size. The whole system can be regarded as a
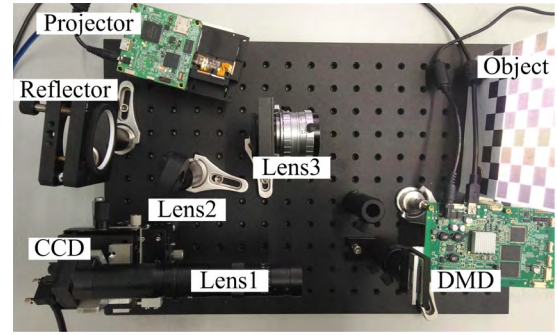

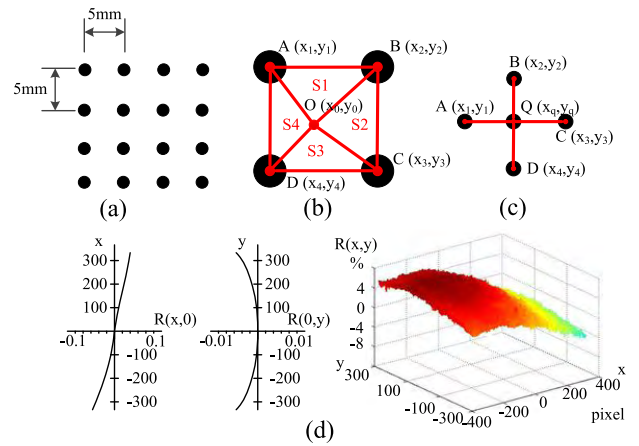**FIGURE 7.** The arrangement of the experimental setup.

FIGURE 8. System calibration and result. (a) The calibration Plane. (b) The calculation of the paraxial magnification in the image center.
(c) Obtaining the paraxial magnifications of every dot. (d) The distortion rate in image coordinate.

camera-projector monocular system where the ordinary camera is replaced by DMD camera with adaptive high dynamic range imaging.

In our experimental setup, lens2, DMD plane and reflector must conform to Scheimpflug condition. This is the major source of imaging distortion. Moreover, traditional radial distortion needs to be considered. To solve the problem of imaging distortion, the procedure of the system calibration is described in the following.

Step1 Capture the image of calibration plane. The calibration plane is a dense dot array printed with a high-quality printer. The distance between two adjacent dots is 5mm, as shown in Fig.8(a).

Step2 Calculate the paraxial magnification of the image center. In captured image, four dots are near the image center $O(x_0, y_0)$, as shown in Fig.8(b). The paraxial magnification of the image center can be expressed by

$$\beta(x_0, y_0) = \beta_{12}\delta_{12} + \beta_{23}\delta_{23} + \beta_{34}\delta_{34} + \beta_{41}\delta_{41} \tag{18}$$

where β_{12}, β_{23}, β_{34} and β_{41} are the paraxial magnification of AB, BC, CD and DA respectively. We can obtain them by the following equations.

$$\beta_{12} = \sqrt{[(x_1 - x_2)^2 + (y_1 - y_2)^2]}/5 \tag{19}$$
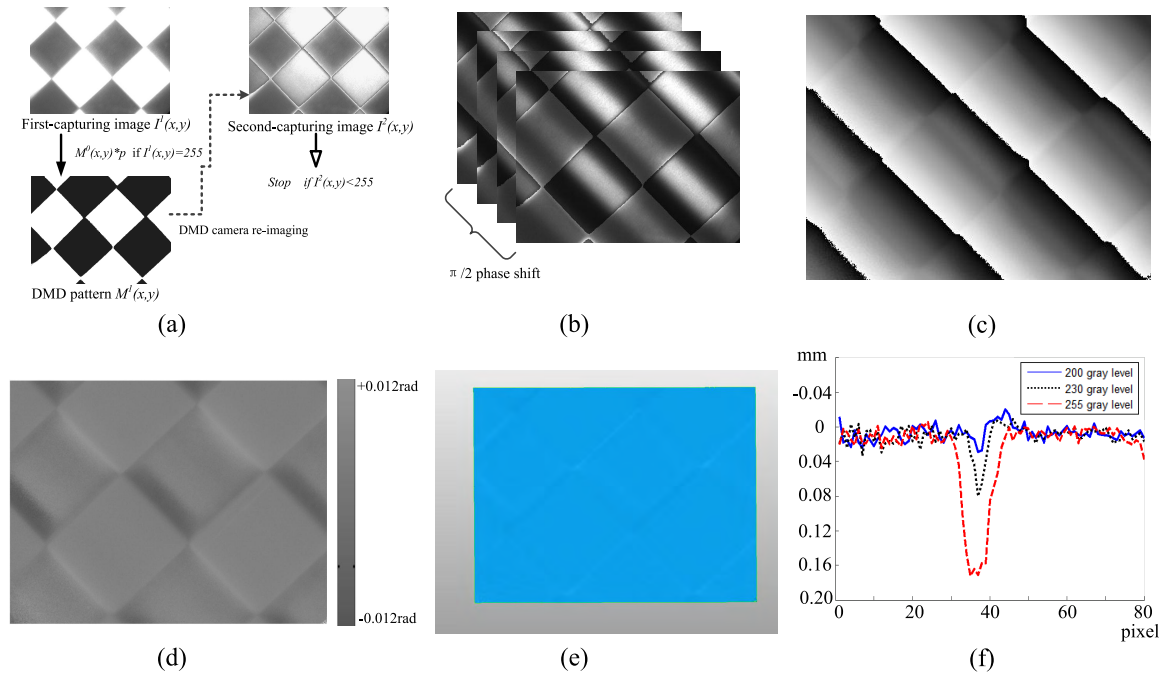
FIGURE 9. Experimental images of measuring the checkerboard. (a) The acquisition process of modulation function. (b) Four phase shifting images after DMD modulation. (c) The wrapped phase distribution. (d) The unwrapped phase difference. (e) The 3-D reconstruction result of the checkerboard. (f) The comparison of the 3-D reconstruction results with different thresholds.

$$\beta_{23} = \sqrt{[(x_2 - x_3)^2 + (y_2 - y_3)^2]/5} \qquad (20)$$

$$\beta_{34} = \sqrt{[(x_3 - x_4)^2 + (y_3 - y_4)^2]/5} \qquad (21)$$

$$\beta_{41} = \sqrt{[(x_4 - x_1)^2 + (y_4 - y_1)^2]/5} \qquad (22)$$

$\delta_{12}, \delta_{23}, \delta_{34}$ and δ_{41} are the weight of $\beta_{12}, \beta_{23}, \beta_{34}$ and β_{41}. We can obtain them by the following equations.

$$\delta_{12} = S_3/(S_1 + S_2 + S_3 + S_4) \qquad (23)$$

$$\delta_{23} = S_4/(S_1 + S_2 + S_3 + S_4) \qquad (24)$$

$$\delta_{34} = S_1/(S_1 + S_2 + S_3 + S_4) \qquad (25)$$

$$\delta_{21} = S_2/(S_1 + S_2 + S_3 + S_4) \qquad (26)$$

where S_1, S_2, S_3, S_4 are the area of the triangles *OAB*, *OBC*, *OCD* and *ODA*, which can be yielded by Heron's formula.

Step3 Obtain the paraxial magnifications of every dot in captured image. Fig.8(c) shows that four dots near dot $Q(x_q, y_q)$. Its paraxial magnification can be obtained by

$$\beta(x_q, x_q) = \sum_{i=1}^{4} \frac{1}{5}\sqrt{[(x_i - x_q)^2 + (y_i - y_q)^2]} \cdot \delta_i \quad (27)$$

where the weight δ_i can be expressed by

$$\delta_i = \frac{\sqrt{(x_{Mod(i+2,4)} - x_q)^2 + (y_{Mod(i+2,4)} - y_q)^2}}{\sum_{i=1}^{4}\sqrt{[(x_i - x_q)^2 + (y_i - y_q)^2]}} \quad (28)$$

Step4 Obtain the paraxial magnifications of other pixels in captured image by bicubic interpolation.

The paraxial magnifications of every pixel will be obtained by above four steps. Distortion rate $R(x, y)$ can be obtained by:

$$R(x, y) = [\beta(x, y) - \beta(x_0, y_0)]/\beta(x_0, y_0) \qquad (29)$$

Fig.8(d) shows the distortion rate $R(x, y)$ in image coordinate. We can correct the distortion in the original images $I(x, y)$ by the following equation:

$$I'(x, y) = I(x, y)/[1 + R(x, y)] \qquad (30)$$

B. THE PERFORMANCE OF PROPOSED METHOD

We measure the B/W flat checkerboard to demonstrate our proposed method first. Fig.9(a) illustrates the adaptive high dynamic range imaging process in which modulation function is acquired. Saturation points in first-capturing image are determined by threshold value of 255. Then the corresponding value in the modulation function is multiplied by a scale factor $p = 0.2$. The scale factor p is predetermined by

$$p = r_{white}/r_{black} \qquad (31)$$

where r_{white} and r_{black} are the reflectivity of the white and black squares respectively.

DMD camera with $M^1(x, y)$ captures the scene image again. Without saturation point in second-capturing image, $M^1(x, y)$ is the final modulation function of DMD camera. Fig.9(b) shows four phase shifting images with the modulation function $M^1(x, y)$. It is obvious that four phase shifting images have no saturation point. So the accurate depth information in sinusoidal waveform is preserved. Fig.9(c) is
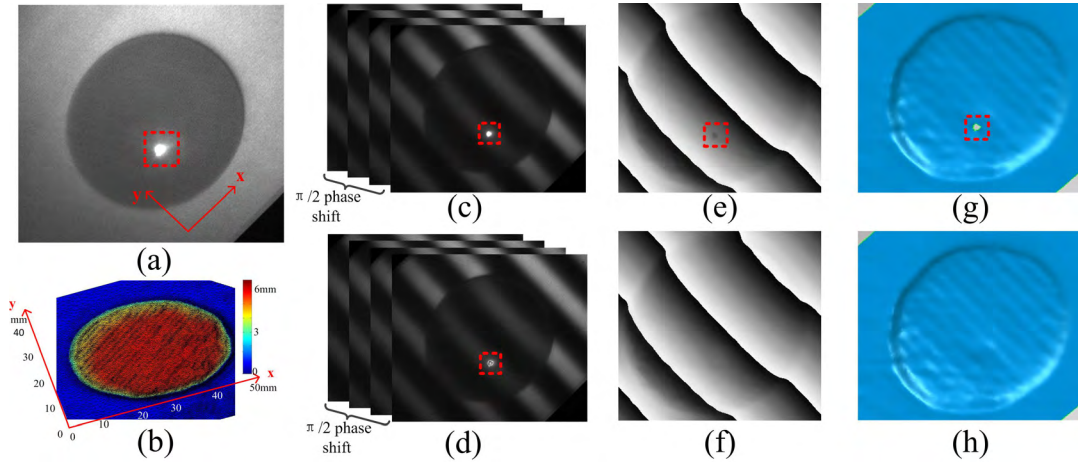
FIGURE 10. Experimental images of measuring the plastic button. (a) The plastic button; (b) the measured result with color mapping. (c) Four fringe images before the DMD modulation. (d) Four fringe images after DMD modulation. (e) The wrapped phase without high dynamic range imaging. (f) The wrapped phase with our adaptive high dynamic range imaging. (g) The 3-D reconstruction result of (e). (h) The 3-D reconstruction result of (f).

the wrapped phase obtained from four phase shifting images by (13). Fig.9(d) is the unwrapped phase difference between the checkerboard and the reference plane. And Fig.9(e) is the 3-D reconstruction result of the checkerboard. The boundaries of the black and white squares are still faintly visible in Fig.9(d) and Fig.9(e). According to above analysis in Section II.A, the notch-like errors are derived from the residual crosstalk glare after the DMD modulation. To discuss the problem, cross-section of the 3-D reconstruction result is shown in Fig.9(f). Here the threshold determining the saturation points is set to different values. The blue solid line, black dot line and red dash line represent the notch-like errors at the threshold = 200, 230, 255 respectively. It can be seen that the notch-like error will decrease with the diminution of the threshold value. In other words, the crosstalk glare will be reduced further with the diminution of the threshold value. But the profile standard deviation/root-mean-square error grows larger on the contrary. So it is necessary to make a tradeoff between the notch-like errors and the profile standard deviation. In most cases, the profile standard deviation is more important to 3D measurement. Furthermore, it is acceptable that the notch-like error is smaller than 0.2mm at threshold value of 255.

We also measure plastic button and metal slice with shiny surface to show the performance of the proposed method. Fig.10 is the measurement images for plastic button. Fig.10(a) is the image of plastic button. The four fringe images with a phase shift of $\pi/2$ are captured before the DMD modulation, as shown in Fig.10(c). The four fringe images with a phase shift of $\pi/2$ are captured after the DMD modulation, as shown in Fig.10(d). The dashed box in Fig.10(d) is the close-up region where the original saturation points are completely eliminated by DMD camera. Fig.10(e) is the wrapped phase without high dynamic range imaging. Fig.10(f) is the wrapped phase with our adaptive high dynamic range imaging. It is obvious that the deformed phase caused by the image

saturation is corrected. Fig.10(g) is the 3-D reconstruction result of plastic button without high dynamic range imaging. In comparison with the 3-D reconstruction result in Fig.10(g), small holes are repaired by our method in Fig.10(h). The final measured result is shown in Fig.10(b).

In another experiment, metal slice is measured, as shown in Fig.11. Different from plastic button, plenty of saturation points concentrate on the edge of the metal slice in Fig.11(a). All fringe images before the DMD modulation contain saturation points in Fig.11(c). In Fig.11(d), these points in the black and white stripes of every phase shifting image are modulated by DMD. Fig.11(e) is the wrapped phase without high dynamic range imaging. The deformed phase is corrected by using our adaptive high dynamic range imaging in Fig.11(f). The relative 3-D reconstruction results are respectively shown in Fig.11(g) and Fig.11(h). Fig.11(g) shows that the deformed phases on the saturation region generate many holes in the process of 3D reconstruction. Fig.11(h) shows that our proposed method reconstructs 3D profile of metal slice well, especially on saturation region. The final measured result is shown in Fig.11(b).

C. ACCURACY EVALUATION
Here, the accuracy in proposed high dynamic range 3D measurement is discussed. The calculation of wrapped phase is the crucial step in 3D measurement. The accuracy of depth coordinate is directly associated with the phase error. By taking the total differential on (13), we can obtain the following equation:

$$d\phi(x, y) = \frac{1}{[I_1(x, y) - I_3(x, y)]^2 + [I_2(x, y) - I_4(x, y)]^2}$$
$$\times \{[I_4(x, y) - I_2(x, y)] \cdot dI_1(x, y) + [I_1(x, y) - I_3(x, y)] \cdot dI_2(x, y) + [I_1(x, y) - I_3(x, y)] \cdot dI_2(x, y) + [I_2(x, y) - I_4(x, y)] \cdot dI_3(x, y)\}$$

$$(32)$$
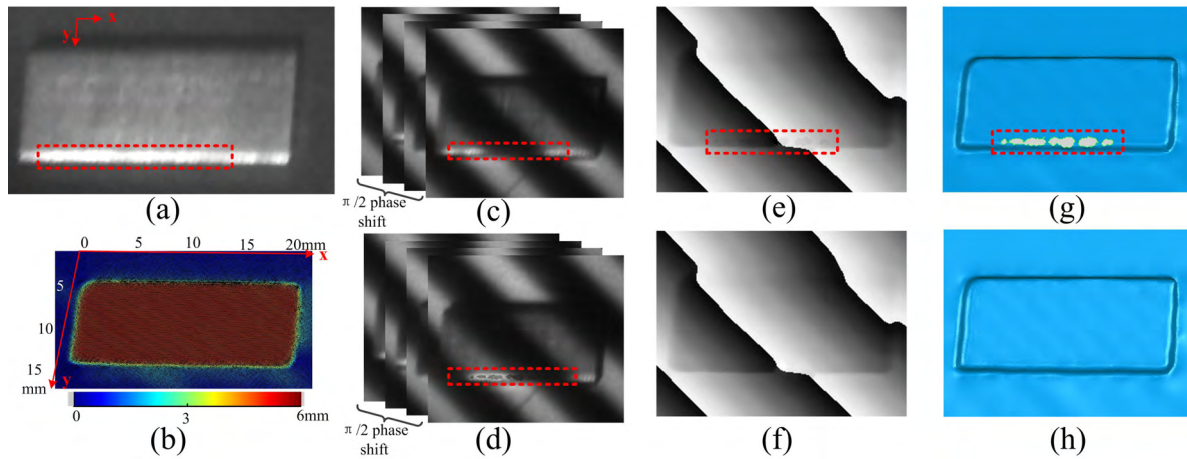
FIGURE 11. Experimental images of measuring the metal slice. (a) The metal slice. (b) The measured result with color mapping. (c) Four fringe images before the DMD modulation. (d) Four fringe images after DMD Modulation. (e) The wrapped phase without high dynamic range imaging. (f) The wrapped phase with our adaptive high dynamic range imaging. (g) The 3-D reconstruction result of (e). (h) The 3-D reconstruction result of (f).

For the sake of simplicity, the image coordinate symbol will be omitted below. Assuming that the quantization errors of captured images conform to the formula:

$$|\Delta I_1| = |\Delta I_2| = |\Delta I_3| = |\Delta I_4| = e \qquad (33)$$

where symbol e is the constant which is associated with A/D convertor of CCD. When the terms dI_1, dI_2, dI_3, dI_4, and $d\phi$ are replaced by the errors ΔI_1, ΔI_2, ΔI_3, ΔI_4 and $\Delta\phi$ respectively, (32) can be rewritten as:

$$\Delta\phi = \frac{2e(|I_1 - I_3| + |I_2 - I_4|)}{(I_1 - I_3)^2 + (I_2 - I_4)^2} \qquad (34)$$

By substituting (14-17) into (34), the phase error based on DMD modulation can be expressed as:

$$\Delta\phi = \frac{\sqrt{2}e(|\sin\phi| + |\cos\phi|)}{M^K b} \qquad (35)$$

where the intensity amplitude b is associated with the response function of CCD and the fringe pattern of projector. As (35) indicates, the bigger the modulation coefficient M^K is, the smaller the phase error $\Delta\phi$ is. However, the modulation coefficient M^K is also limited by the demand for saturation avoidance. So we need to make a tradeoff in selecting the modulation coefficient, i.e., the modulation coefficient is selected as big as possible on the premise that saturation points can be completely eliminated. In actual experiment, the modulation coefficient in saturation point is determined by the selected scale factor p. So the relations between the phase error and different scale factors are analyzed here. In the 3D measurement experiment of metal slice, the phase errors and modulation times with the scale factor from 0.01 to 0.9 is recorded, as shown in Fig.12. With the increasement of scale factor, Phase errors represented by the red solid line will decrease, and modulation times represented by blue dash line will grow larger. In order to ensure the accuracy of phase error
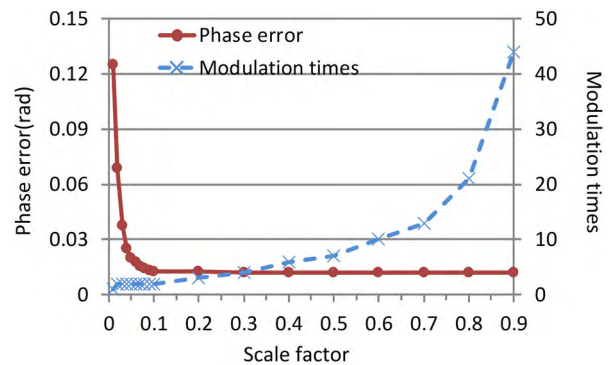
FIGURE 12. Phase errors and modulation times at different scale factors.

TABLE 1. The comparative results of three methods.

	Number of captured images [a]	Total processing time (s)	Measuring error (mm)	
			maximum	RMS
Liu's method	4K	4.37	1.09	0.033
Li's method	4K	5.15	0.87	0.029
Our method	4+K	1.97	0.18	0.021

[a]Assume that the saturation in the image is eliminated in the K th time

and the efficiency of saturation avoidance, it is reasonable to select the scale factor from 0.05 to 0.5. In addition, Increasing N will not affect the phase accuracy, but it will be limited by DMD pixel number. If DMD pixel number is not enough to assign to all CCD pixels, the measuring accuracy will be affected.

To verify the advantage in the accuracy and the efficiency, our proposed method is compared with two widespread HDR measurement methods proposed by Gui-hua Liu and Li Rao [12], [24]. The metal slice in Fig.11 is measured by

three methods. The comparison experiment is implemented in the same apparatuses such as CCD, projector and PC. To obtain the measuring error, the metal slice is measured by coordinate measuring machine (MITUTOYO – B403B) with a precision of 0.002mm. We regard the measuring data of coordinate measuring machine as the truth value. The results of these calculations are given in Table 1. In Liu's method and Li's method, multiple sets of fringe images are acquired by changing the exposure time of CCD and controlling the projected fringe pattern intensities respectively. However, our method only needs to capture four phase shifting images and K modulation images, which saves the processing time observably. In addition, since the crosstalk glare is eliminated availably, the measuring accuracy in the saturation region is enhanced.

IV. CONCLUSION

In this works, we described an adaptive high dynamic range three-dimensional shape measurement using DMD camera. Specially, imaging characteristics of the surface with high reflectivity variation was summarized by analyzing the bidirectional reflectance distribution function and the crosstalk on CCD chip. On the basic of the theory, we developed the strategy that DMD modulation function is determined to avoid saturation prior to the acquisition of phase shifting images. The experimental results verify that proposed method is suitable for the object with high reflectivity variation, such as B/W checkerboard, metal parts, and plastic products. Furthermore, compared with other multiple exposure methods, proposed method has obvious advantages in the number of captured images and the avoidance of pixel crosstalk.

REFERENCES

[1] Y. Hu, Q. Chen, S. Feng, T. Tao, A. Asundi, and C. Zuo, "A new microscopic telecentric stereo vision system—Calibration, rectification, and three-dimensional reconstruction," *Opt. Lasers Eng.*, vol. 113, pp. 14–22, Feb. 2019.

[2] E. Latorre, S. Kale, and L. Casares, M. Gómez-GonzÃₐlez, M. Uroz, L. Valon, R. V. Nair, E. Garreta, N. Montserrat, A. del Campo, B. Ladoux, M. Arroyo, and X. Trepat, "Active superelasticity in three-dimensional epithelia of controlled shape," *Nature*, vol. 563, no. 7730, pp. 203–208, Nov. 2018.

[3] A. Brahm, R. Ramm, S. Heist, C. Rulff, P. Kühmstedt, and G. Notni, "Fast 3D NIR systems for facial measurement and lip-reading," *Proc. SPIE*, vol. 10220, May 2017, Art. no. 102200P.

[4] S. Feng, L. Zhang, C. Zuo, T. Tao, Q. Chen, and G. Gu, "High dynamic range 3D measurements with fringe projection profilometry: A review," *Meas. Sci. Technol.*, vol. 29, no. 12, Dec. 2018, Art. no. 122001.

[5] H. Lin, J. Gao, G. Zhang, X. Chen, Y. He, and Y. Liu, "Review and comparison of high-dynamic range three-dimensional shape measurement techniques," *J. Sensors*, vol. 2017, Apr. 2017, Art. no. 9576850.

[6] H.-Y. Tu and S.-C. He, "Fringe shaping for high-/low-reflectance surface in single-trial phase-shifting profilometry," *Chin. Opt. Lett.*, vol. 16, no. 10, Oct. 2018, Art. no. 101202.

[7] Z. Qi, Z. Wang, J. Huang, C. Xing, and J. Gao, "Invalid-point removal based on epipolar constraint in the structured-light method," *Opt. Lasers Eng.*, vol. 105, pp. 173–181, Jun. 2018.

[8] C. Chen, N. Gao, X. Wang, and Z. Zhang, "Adaptive pixel-to-pixel projection intensity adjustment for measuring a shiny surface using orthogonal color fringe pattern projection," *Meas. Sci. Technol.*, vol. 29, no. 5, May 2018, Art. no. 055203.

[9] Z. Qi, Z. Wang, J. Huang, C. Xing, and J. Gao, "Error of image saturation in the structured-light method," *Appl. Opt.*, vol. 57, no. 1, pp. A181–A188, Jun. 2018.

[10] C. Waddington and J. Kofman, "Camera-independent saturation avoidance in measuring high-reflectivity-variation surfaces using pixel-wise composed images from projected patterns of different maximum gray level," *Opt. Commun.*, vol. 333, pp. 32–37, Dec. 2014.

[11] S. Feng, Q. Chen, C. Zuo, and A. Asundi, "Fast three-dimensional measurements for dynamic scenes with shiny surfaces," *Opt. Commun.*, vol. 382, pp. 18–27, Jan. 2017.

[12] G.-H. Liu, X.-Y. Liu, and Q.-Y. Feng, "3D shape measurement of objects with high dynamic range of surface reflectivity," *Appl. Opt.*, vol. 50, no. 23, pp. 4557–4565, Aug. 2011.

[13] J. Lin, K. Jiang, and M. Chang, "A novel solution for camera occlusion in stereo vision technique," *Adv. Mech. Eng.*, vol. 5, Jan. 2013, Art. no. 253794.

[14] Y. Chen, Y. He, and E. Hu, "Phase deviation analysis and phase retrieval for partial intensity saturation in phase-shifting projected fringe profilometry," *Opt. Commun.*, vol. 281, no. 11, pp. 3087–3090, Jun. 2008.

[15] B. Chen and S. Zhang, "High-quality 3D shape measurement using saturated fringe patterns," *Opt. Lasers Eng.*, vol. 87, pp. 83–89, Dec. 2016.

[16] M. Wang, G. Du, C. Zhou, C. Zhang, S. Si, H. Li, Z. Lei, and Y. Li, "Enhanced high dynamic range 3D shape measurement based on generalized phase-shifting algorithm," *Opt. Commun.*, vol. 385, pp. 43–53, Feb. 2017.

[17] S. Zhang and S.-T. Yau, "High dynamic range scanning technique," *Opt. Eng.*, vol. 48, no. 3, Mar. 2009, Art. no. 033604.

[18] H. Lin, J. Gao, Q. Mei, Y. He, J. Liu, and X. Wang, "Adaptive digital fringe projection technique for high dynamic range three-dimensional shape measurement," *Opt. Express*, vol. 24, no. 7, pp. 7703–7718, Apr. 2016.

[19] I. Popadic, B. M. Todorović, and I. Reljin, "Method for HDR-like imaging using industrial digital cameras," *Multimed Tools Appl.*, vol. 76, no. 10, pp. 12801–12817, May 2017.

[20] P. Kuhmstedt, C. Bräuer-Burchardt, S. Heist, I. Schmidt, and G. Notni, "GOBO projection for underwater 3D measurement technique," in *Proc. SPIE* vol. 10329, Jun. 2017, Art. no. 103290N.

[21] Z. Qi, Z. Wang, J. Huang, Q. Xue, and J. Gao, "Improving the quality of stripes in structured-light three-dimensional profile measurement," *Opt. Eng.*, vol. 56, no. 6, Mar. 2009, Art. no. 031208.

[22] C. Chen, N. Gao, X. J. Wang, and Z. Zhang, "Adaptive projection intensity adjustment for avoiding saturation in three-dimensional shape measurement," *Opt. Commun.*, vol. 410, pp. 694–702, Mar. 2018.

[23] D. Li and J. Kofman, "Adaptive fringe-pattern projection for image saturation avoidance in 3D surface-shape measurement," *Opt. Express*, vol. 22, no. 8, pp. 9887–9901, Apr. 2014.

[24] L. Rao and F. Da, "High dynamic range 3D shape determination based on automatic exposure selection," *J. Vis. Commun. Image Represent.*, vol. 50, pp. 217–226, Jan. 2018.

[25] A. A. Adeyemi, N. Barakat, and T. E. Darcie, "Applications of digital micro-mirror devices to digital optical microscope dynamic range enhancement," *Opt. Express*, vol. 17, no. 3, pp. 1831–1843, Feb. 2009.

[26] S. Ri, M. Fujigaki, and Y. Morimoto, "Single-shot three-dimensional shape measurement method using a digital micromirror device camera by fringe projection," *Proc. SPIE*, vol. 48, no. 10, Oct. 2009, Art. no. 103605.

[27] B. Blanco-Filgueira, P. López, and J. B. Roldán, "Closed-form and explicit analytical model for crosstalk in CMOS photodiodes," *IEEE Trans. Electron Devices*, vol. 60, no. 10, pp. 3459–3464, Oct. 2013.

[28] T. Lin, R. Olah, and A. K. Dutta, "Effect of dense planer focal plane array on device performances," *Proc. SPIE*, vol. 9100, Jun. 2014, Art. no. 91000K.

[29] S.-B. Zhao, F.-M. Zhang, X.-H. Qu, Z. Chen, and S.-W. Zheng, "Removal of parasitic image due to metal specularity based on digital micromirror device camera," *Opt. Eng.*, vol. 53, no. 6, Jun. 2014, Art. no. 063105.

[30] S.-B. Zhao, M.-Y. Ma, and C. Guo, "Accurate pixel-to-pixel alignment method with six-axis adjustment for computational photography," *IEEE Photon. J.*, vol. 10, no. 3, Jun. 2018, Art. no. 6802416.

SHOU-BO ZHAO received the B.S. and Ph.D. degrees in optical engineering from Tianjin University, in 2008 and 2015, respectively. Since 2015, he has been a Lecturer with the Higher Educational Key Laboratory for Measuring and Control Technology and Instrumentations of Heilongjiang Province, Harbin University of Science and Technology, China. His research interests include optical metrology using image processing and computational camera development.

MING-YANG MA received the B.S. degree in communication engineering from Liaocheng University, Liaocheng, in 2017. He is currently pursuing the M.S. degree in electronics and communication engineering with the Harbin University of Science and Technology, Harbin, China. He has authored two papers. He holds three patents. His research interests include image processing and compression sensing techniques using DMD cameras.

● ● ●
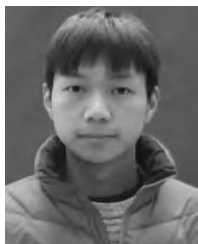
LI-YUAN LIU received the B.S. degree in measurement and control technology and instruments from Northeast Petroleum University, Daqing, in 2017. He is currently pursuing the M.S. degree in measurement and control technology and communication engineering from the Harbin University of Science and Technology, Harbin, China. His research interests include visual detection and image processing.